communications
earth & environment

ARTICLE

https://doi.org/10.1038/s43247-023-01028-5 OPEN

Replacement reactions for carbon geosequestration may be faster in calcium olivine vs magnesium olivine

Hsieh Chen[1]✉

CO_2 mineralization is the safest CO_2 geosequestration method with the highest sequestration capacity. Even though there have been lab and pilot-scale demonstrations, the complex chemical reaction is still elusive at atomic level. Here, I show that the ab initio molecular dynamics (AIMD) and metadynamics simulations enable quantitative analysis of reaction pathways, thermodynamics, and kinetics of the Mg^{2+} and Ca^{2+} ion dissolutions from olivine minerals, which have high weathering potential for carbonation process. The leaching of Ca^{2+} from the Ca-olivine surface is a ligand exchange process that results in a much lower energy barrier with 10^3 times faster dissolution rate compared to the leaching of Mg^{2+}, which the tight magnesium sites on the forsterite (Mg-olivine) surface forbid ligand exchange. These results provide indication on water capabilities in solvating Ca^{2+} and Mg^{2+} that are relevant to mineral carbonation and can help the evaluation of potential enhanced CO_2 mineralization mechanisms.

---

[1] Aramco Americas: Aramco Research Center-Boston, 400 Technology Square, Cambridge, MA 02139, USA. ✉email: hsieh.chen@aramcoamericas.com

Anthropogenic CO_2 cumulation in atmosphere since industry revolution is estimated to reach 2,000 gigatons ($GtCO_2$), and the CO_2 emissions are reaching 40 $GtCO_2$ per year today. To offset the CO_2 emissions to avoid the worst impacts of climate crisis, we need to develop technologies targeting the removal of CO_2 in the order of $GtCO_2$ per year. Unfortunately, the most mature current practices for storing CO_2 in sedimentary formations such as abandoned oil and gas reservoirs or CO_2-enhanced oil recovery can only remove in the order of tens of $MtCO_2$ per year (0.01 $GtCO_2$ per year) at best. Furthermore, it is estimated that the total CO_2 storage capacity for the depleted oil and gas reservoirs globally is around 675–900 $GtCO_2$, which is insufficient for offsetting the long-term global emissions. On the other hand, storage capacities of underground saline aquifers and mineralization in igneous rock formations high in divalent cations are estimated to be 25,000 $GtCO_2$ and 60,000,000 $GtCO_2$, respectively, which are more than enough to sequestrate all the undesirable CO_2 if the resources are economically accessible with appropriate technology[1–4].

CO_2 mineralization geosequestration is a promising CO_2 storage method with the highest storage capacity. In addition, it is considered very safe because the mineralized CO_2 has no leakage issues compared to storing in sedimentary reservoir rocks with structural and stratigraphic trapping mechanisms[1–4]. The lab demonstrations of CO_2 mineralization with contact of silicate minerals high in divalent ions have been conducted more than two decades ago and have been an active research area[5–10]. Different reaction conditions such as the temperatures, CO_2 partial pressures, solution ion compositions, pH, silicate particle sizes, reaction times can all affect the CO_2 mineralization. In addition, the thermodynamics, aggregation state, and density of CO_2 can affect the speed of mineral carbonation. For example, Calcara and Caricaterra developed a model to correlate the CO_2 dipole moment and density, which can explain the accelerated mineralization in dense gaseous, liquid and supercritical CO_2 ($scCO_2$) observed experimentally[11]. Nevertheless, the detailed kinetics and mechanism of how the carbonation proceeds are still not very clear (except for very few works as for example Regnault et al. [12]).

The most prominent pilot-scale field demonstrations for CO_2 mineralization geosequestration to date are the CarbFix project[13–16] in Southwest Iceland and the Wallula project[17–19] in the Columbia River Basalt Group (CRBG) of southeastern Washington State, USA. Two years after injections, the Carbfix project and the Wallula project have reported between 72% and 95% (57–75 tCO_2 per year) and 60% (293 tCO_2 per year) mineralization of injected CO_2, respectively. Due to the complex mineralogy and large number of geochemical dissolution reactions occurred at the test sites, the predictions of the CO_2 mineralization process have been difficult despite the promising field test results[20–24].

Molecular-level mechanistic insight can complement the macroscopic observables for the fundamental understanding of the CO_2 mineralization process and provide quantitative predictions for the reaction rates and mechanisms. For example, Criscenti and Cygan used classical molecular dynamics simulations to compare the solvation energies of alkali and alkaline-earth metal cations in water and liquid CO_2, which can help to understand the partitioning of metal cations between aqueous solutions and $scCO_2$ where limited experimental data exist[25]. In aqueous carbonation process, the CO_2 mineralization steps include CO_2 solvation, CO_2 speciation, mineral dissolution, ion-pair formation, nucleation, and growth[26]. When comparing the energy barriers and reaction rates for each step, it is postulated that the mineral dissolution is the rate-limiting step. Indeed, early studies have shown the strong correlation between mineralization time scales and the rock dissolution rates across lab to geological times (from 0.001 to 10^7 years)[27]. Thus, in this work I would focus on studying the mineral dissolution step. There have been molecular simulations to study the solubility as well as the diffusion of CO_2 in water films[28,29], which are very interesting studies that complement the present work.

Forsterite (Mg-olivine) is one of the most abundant silicates in the Earth's upper mantle and is considered a promising mineralogy for CO_2 mineralization geosequestration because of its prominent occurrence and its high reactivity with water and CO_2. Ca-olivine, however, is a rare mineral. That is to say, real in-situ experimental results point out the importance of Calcium: CarbFix Calcite, Wallula (with $scCO_2$) Ankerite ($CaFe(CO_3)_2$). Namely, ref. [17] indirectly points out a probable major mobility of Ca. Already present in formation waters, its ionic concentration grows more than Mg as soon as CO_2 is injected. Reference [19] points out the principal product of the in-situ experiment: Ankerite (a Ca/Fe rich carbonate). So, to understand the formation of calcium and magnesium carbonates evidenced by in-situ experiences, starting from silicate leaching, I would study Mg and Ca mobility with AIMD and metadynamics simulations for the dissolution of Mg-olivine and Ca-olivine. To the best of my knowledge, this is the first study that quantitively predicted the mineral dissolution energy barriers and reaction rates from computational quantum chemistry in CO_2 mineralization geosequestration.

Results

The simulated systems are the Mg-olivine and Ca-olivine (010) surfaces. Figure 1 shows the molecular model of the Mg-olivine. The Ca-olivine has the same molecular structure as in Fig. 1

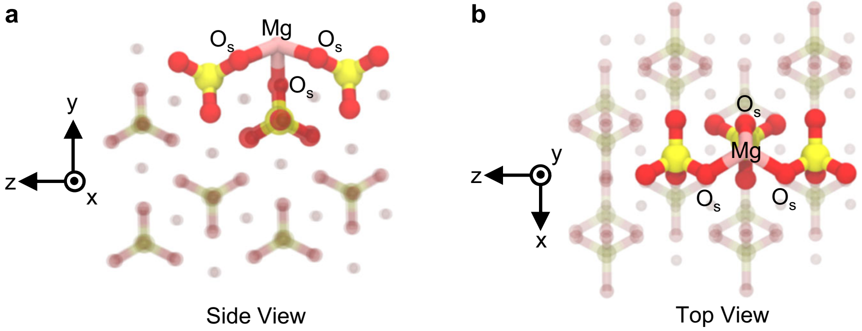

Fig. 1 Mg-olivine surface molecular model. **a** Side view and **b** top view of the Mg-olivine (010) surface molecular model. The Mg atoms are colored in pink, O atoms in red, and Si atoms in yellow. One surface Mg atom bonded with 3 surface silicates (SiO_4) through silicate oxygen atoms (O_s) are highlighted with solid colors while other atoms are colored with transparent colors.

although with slightly different lattice sizes because of the larger Ca ionic radius. About 20 Å of neutral water layers are placed on the mineral surfaces followed by 15 Å vacuum gaps in the *y* direction to avoid spurious interactions in three-dimensional periodic boundary conditions. AIMD simulations are performed in the Canonical *NVT* ensemble with constant number of atoms *N* (32 Mg or Ca cations, 16 SiO_4 anions, and 65 H_2O molecules), constant volume of simulation box *V*, and constant temperature *T* of 300 K. At least 5 ps of nonbiased simulations are performed to equilibrate the mineral-water interfaces before biased simulations with metadynamics enhanced sampling to acquire the free energy landscapes for the dissolution of Mg-olivine and Ca-olivine. In metadynamics, 3 coordination numbers (CNs) are tracked: (1) CN(M-O_s) for metal cation surface bonding, where M stands for Ca or Mg and O_s stands for mineral surface oxygen (see Fig. 1), (2) CN(M-O_w) for metal cation hydration, where O_w stands for water oxygen, and (3) CN(O_s-H) for the protonation of mineral surface oxygens, where H stands for water hydrogen. See Methods for simulation details. In the following subsections I will first show the dissolution of Mg-olivine, then the dissolution of Ca-olivine.

Dissolution of Mg-olivine. Figure 2 shows the time evolutions of the 3 CNs through the 336 ps AIMD metadynamics simulations for Mg-olivine dissolution. As shown, the surface bonds start to break (CN(Mg-O_s) = ~3 to ~1) around 150 ps with increasing hydration numbers (CN(Mg-O_w) = ~3 to ~5). With further simulation time, all the CNs start to be able to sample wider ranges, indicating the metadynamics simulation is headed toward convergence.

Figure 3a shows the 3D free energy surface as calculated with AIMD metadynamics for the Mg-olivine dissolution, and Fig. 3b shows the minimum free energy path. The first notable step is for the protonation of one surface silicate oxygen atom combining with adding one hydration number to Mg from State A to State B. See Table 1 for the CNs of each state of the Mg-olivine dissolution process. Note that in the present simulation with neutral water, the protonation of mineral surface oxygen is accompanied by water dissociation with the remaining OH^- diffuses into the water layer. The total energy spent from State A to State B is about 9 kJ mol^{-1} (Fig. 3b). This observation is consistent with early studies: the olivine dissolution is facilitated in acidic condition where more mineral surface oxygens are in the protonated state[30].

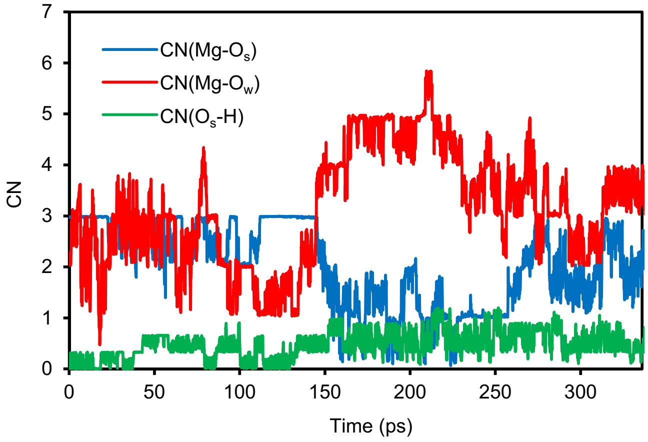

Fig. 2 Time evolutions of the 3 CNs through the 336 ps AIMD metadynamics simulations for Mg-olivine dissolution. The blue curve is the Mg bonds with surface silicates, CN(Mg-O_s); the red curve is the Mg hydration, CN(Mg-O_w); and the green curve is the protonation of surface silicates, CN(O_s-H).

The second notable step is the actual dissolution of Mg from surface by breaking two Mg-O_s coordination from State C to State D (Table 1). Here, the bond breaking happens without any extra hydration (where CN(Mg-O_w) = 3 in both States C and D) that results in higher energy barrier, which is very different from the case for Ca-olivine dissolution (details later). The AIMD simulation snapshots for the State C and State D are shown in Fig. 4. The highest energy barrier that is also the rate limiting step for the Mg dissolution in acid-like condition (implicitly, more surface oxygens are in the protonated state, CN(O_s-H) = 0.33) is estimated to be E_a(Mg) = 59 kJ mol^{-1} (Fig. 3b from State C to State D). Finally, from State D to State G (Table 1) the Mg ion gains two extra hydration numbers and the surface silicate oxygens gain another protonation to lower the total energy in the system, yet the Mg ion is not completely detached from surface (CN(Mg-O_s) = 1 in States D, E, F, and G) before the end of the simulations. Note that O_s is bonded with Si during the entire simulation runs (see Fig. 4) because of the strong silicon-oxygen bonds in the silicate anions.

Dissolution of Ca-olivine. Figure 5 shows the time evolutions of the 3 CNs through the 186 ps AIMD metadynamics simulations for Ca-olivine dissolution. As shown, the surface bonds start to break (CN(Ca-O_s) = ~3 to ~1) around 60 ps with increasing hydration numbers (CN(Ca-O_w) = ~4 to ~7). With further simulation time, all the CNs start to be able to sample wider ranges, indicating the metadynamics simulation is headed toward convergence.

Figure 6a shows the 3D free energy surface as calculated with AIMD metadynamics for the Ca-olivine dissolution, and Fig. 6b shows the minimum free energy path. The first notable step is again for the protonation of one surface silicate oxygen atom from State A to State B. See Table 2 for the CNs of each state of the Ca-olivine dissolution process. In fact, State B has lower energy than State A suggests that at energy minimum the surface silicate oxygen would be in the protonated state, which was observed in prior study[31]. The actual dissolution of Ca ion from surface can be divided into the following sub steps (Table 2): (1) From State B to State C, the system breaks one Ca-O_s bond while gains one extra hydration Ca-O_w. (2) From State C to State D, the system breaks the second Ca-O_s bond while gains the second extra hydration Ca-O_w. (3) From State D to State E, the system gains the third extra hydration Ca-O_w. The AIMD simulation snapshots for States B, C, D, and E are shown in Fig. 7. The Ca dissolution process with the addition of 3 extra hydration results in a lower activation energy compared to the Mg dissolution process. The activation energy for Ca-olivine dissolution is estimated to be E_a(Ca) = 39 kJ mol^{-1} (Fig. 6b from State B to State E). The larger size of the Ca ion allows for the extra hydrations during the dissolution process while the smaller size of the Mg ion disallows for the extra hydrations during the dissolution process (cf. Figs. 4 and 7), which is the molecular origin for the different ion specific dissolution energy barriers. Finally, from State E to State H (Table 2) the Ca ion is fully detached from the surface (CN(Ca-O_s) = 0) with 6 to 8 hydration numbers (CN(Ca-O_w) = 6 to 8) with lowered system energies.

Discussion

I have obtained the activation energies for the dissolution of Mg-olivine and Ca-olivine in acid-like condition (CN(O_s-H) = 0.33) that is relevant to CO_2 mineralization geosequestration to be E_a(Mg) = 59 kJ mol^{-1} and E_a(Ca) = 39 kJ mol^{-1}. Using the Arrhenius equation, I can relate the activation energies to the rate

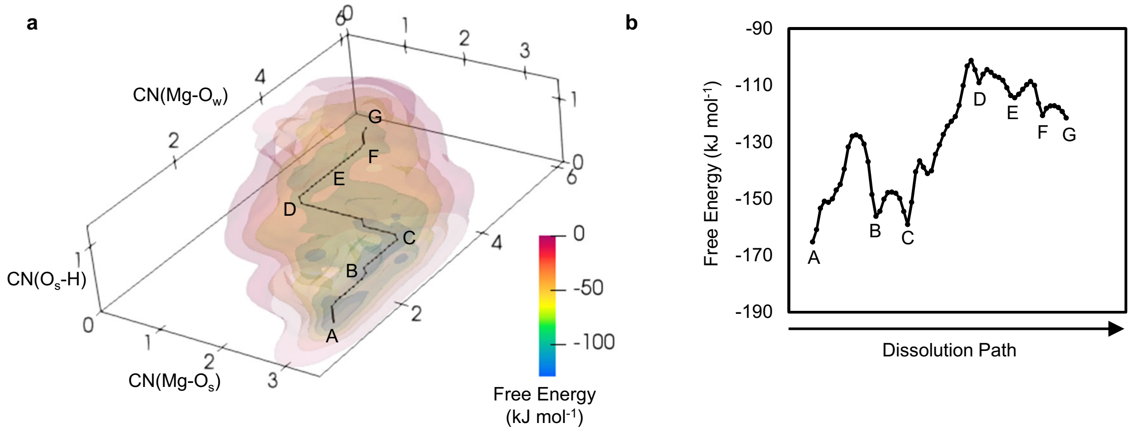

Fig. 3 Free energy landscapes for Mg-olivine dissolution. **a** 3D free energy surface and **b** minimum free energy path for Mg-olivine dissolution. See Table 1 for the CNs of each state.

Table 1 CNs of each state of the Mg-olivine dissolution process.

State	CN(Mg-O$_s$)	CN(Mg-O$_w$)	CN(O$_s$-H)
A	3	1	0
B	3	2	0.33
C	3	3	0.33
D	1	3	0.33
E	1	4	0.33
F	1	5	0.33
G	1	5	0.67

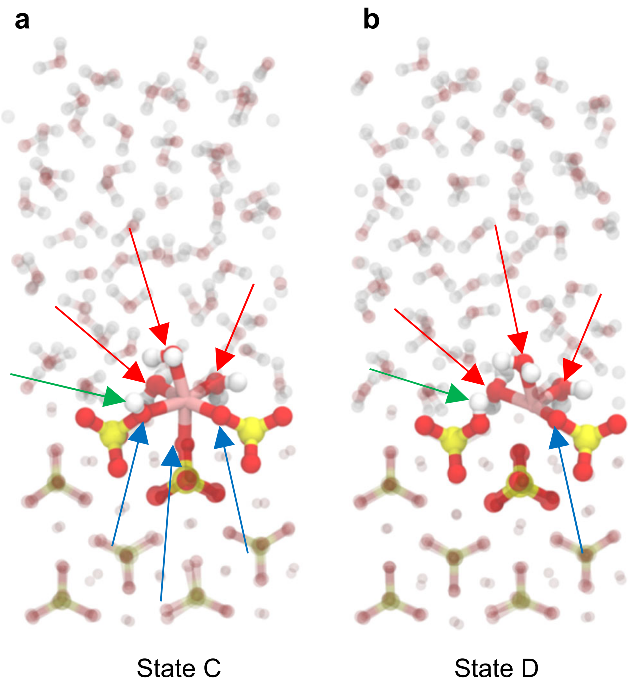

Fig. 4 AIMD simulation snapshots for Mg-olivine dissolution. **a** State C and **b** State D of Mg-olivine dissolution. See Table 1 for the CNs of each state. The atom colors are Mg = pink; Si = yellow; O = red; H = white. The surface Mg atom with bonded surface silicate ions and water molecules are drawn in solid colors while other atoms are drawn in transparent colors. The red, blue, and green arrows show the Mg-O$_w$, Mg-O$_s$, and O$_s$-H bonds, respectively.

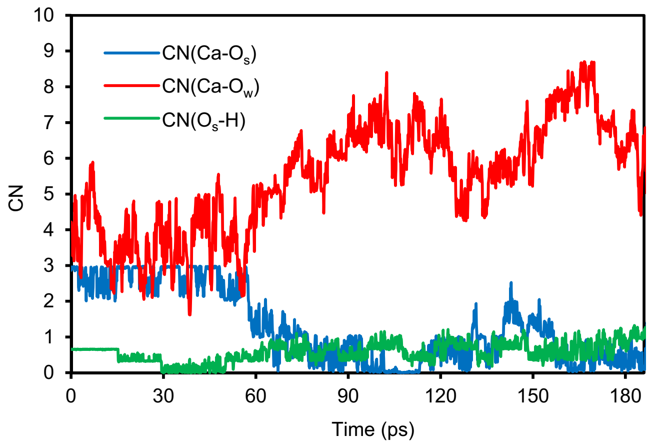

Fig. 5 Time evolutions of the 3 CNs through the 186 ps AIMD metadynamics simulations for Ca-olivine dissolution. The blue curve is the Ca bonds with surface silicates, CN(Ca-O$_s$); the red curve is the Ca hydration, CN(Ca-O$_w$); and the green curve is the protonation of surface silicates, CN(O$_s$-H).

constant,

$$k = Ae^{\frac{-E_a}{RT}}, \tag{1}$$

where A is the pre-exponential factor, R is the universal gas constant, and T is the temperature. Assuming the pre-exponential factor A is similar for both Mg-olivine and Ca-olivine dissolution (which is reasonable because of the similar bond breaking process on the mineral surfaces), the ratio of the rate constants for Mg-olivine and Ca-olivine dissolution can then be calculated as

$$\frac{k(\mathrm{Ca})}{k(\mathrm{Mg})} \sim e^{\frac{E_a(\mathrm{Mg})-E_a(\mathrm{Ca})}{RT}} \sim 3\times 10^3, \tag{2}$$

using $R = 8.314\ \mathrm{J\,mol^{-1}\,K^{-1}}$ and $T = 300$ K. There have been direct measurements for the dissolution rates of natural or synthetic orthosilicate minerals with chemical compositions and structures like olivine[30]. With the rate constants of γ-Ca_2SiO_4 (Ca-olivine) dissolution and Mg_2SiO_4 (Mg-olivine) dissolution measured to be $k(\mathrm{Ca}) = 2.0 \times 10^{-9}\ \mathrm{mol\,cm^{-2}\,s^{-1}}$ and $k(\mathrm{Mg}) = 7.5 \times 10^{-13}\ \mathrm{mol\,cm^{-2}\,s^{-1}}$, the experimental ratio is $k(\mathrm{Ca})/k(\mathrm{Mg}) = 2.7 \times 10^3$ that is very similar to the ratio predicted from AIMD simulations. In addition, recent in-situ experiments have measured the apparent activation energies for the forsterite

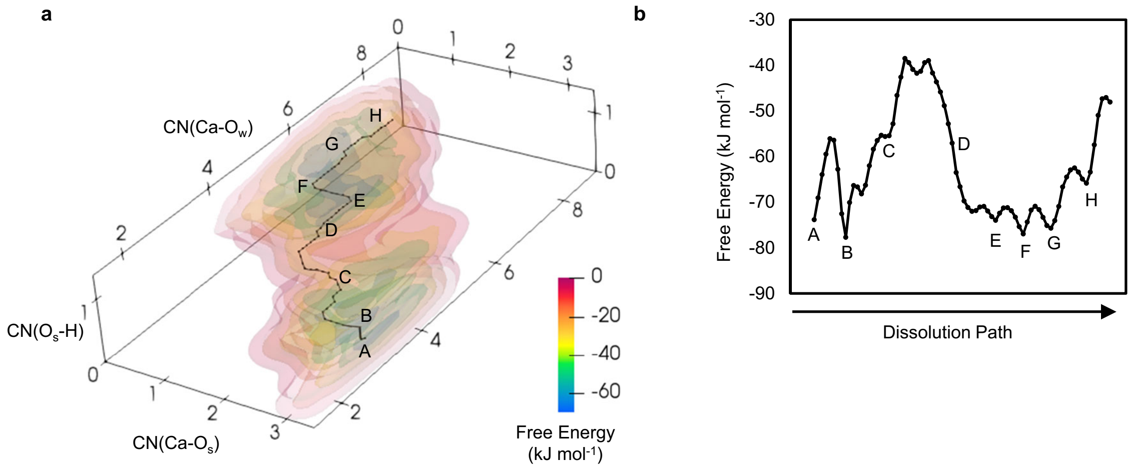

Fig. 6 Free energy landscapes for Ca-olivine dissolution. **a** 3D free energy surface and **b** minimum free energy path for Ca-olivine dissolution. See Table 2 for the CNs of each state.

Table 2 CNs of each state of the Ca-olivine dissolution process.

State	CN(Ca-O$_s$)	CN(Ca-O$_w$)	CN(O$_s$-H)
A	3	3	0
B	3	3	0.33
C	2	4	0.33
D	1	5	0.33
E	1	6	0.33
F	0	6	0.33
G	0	7	0.33
H	0	8	0.33

(Mg_2SiO_4) to magnesite ($MgCO_3$) carbonation to be $E_a(\mathrm{Mg}) = 34$ to 130 kJ mol^{-1} at different relative humidity and temperature ranges[6–10,26]. The simulation results are within these values and can provide insight into the independent carbonation steps for the integrated carbonation process.

Conclusions

In summary, using AIMD and metadynamics simulations, I have calculated the free energy landscapes for the Mg^{2+} and Ca^{2+} ion dissolutions from olivine minerals. The leaching of Ca^{2+} from the Ca-olivine surface is a ligand exchange process with an energy barrier of $E_a(\mathrm{Ca}) = 39$ kJ mol^{-1}; in contrast, the leaching of Mg^{2+} from the Mg-olivine surface has a higher energy barrier of $E_a(\mathrm{Mg}) = 59$ kJ mol^{-1} due to the tight magnesium sites on the Mg-olivine surface that forbid ligand exchange. Furthermore, the predicted ion specific dissolution rate ratio, $k(\mathrm{Ca})/k(\mathrm{Mg}) \sim 3 \times 10^3$, agrees with available experimental data from the direct dissolution rate measurements. To the best of my knowledge, this is the first study that quantitively predicts the mineral dissolution energy barriers and reaction rates from computational quantum chemistry in CO_2 mineralization geosequestration. I believe the present study can provide the following insights: (1) Provide indication on water capabilities in leaching and solvating Ca^{2+} and Mg^{2+}, which are important ions in mineral carbonation[32–35]. (2) Help adjust kinetic parameters for macroscopic CO_2 sequestration simulations and operations in lab and field applications[36–38]. (3) Evaluate potential ex-situ mitigation methods for accelerating the CO_2 mineralization process based on their kinetic reaction pathways[39–42].

Methods

Olivine surface molecular models. The olivine non-dipolar (010) surface has been identified as the most stable surface, corresponding to its main mineralogical cleavage plane[43,44]. I select a 2 × 2 (010) surface unit cell representatively shown in Fig. 1 for all the calculations. Nevertheless, other low energy olivine surfaces such as (100) surface[45] may also worth exploring. In this work, perfect crystal surfaces are used as starting points for the mineral dissolution process. How the presence of olivine surface defects[46] such as oxygen vacancies would affect the dissolution process is a very interesting topic for future work. The olivine surface models consist of 32 divalent cations (32 Mg atoms for Mg-olivine or 32 Ca atoms for Ca-olivine) and 16 SiO_4 anions. 65 H_2O molecules with a water layer thickness of around 20 Å are then placed on top of the surfaces. Totally, 307 atoms with 32 Mg or Ca atoms, 16 Si atoms, 129 O atoms, and 130 H atoms are used in each simulation systems. Simulation boxes with 3D periodic boundary conditions of sizes 9.498 Å × 45.1985 Å × 11.9584 Å and 10.162 Å × 45.1985 Å × 13.556 Å are used for Mg-olivine and Ca-olivine simulations, respectively, with vacuum gaps of around 15 Å between the top of the water films and the bottom of the periodic image of the olivine slabs in the *y* direction. The lattice parameters for the Mg-olivine and Ca-olivine are took from early Density Functional Theory (DFT) simulations that are consistent with experiments[31]. Similar vacuum gap sizes have been used in early DFT simulations, which have been shown to be sufficient to eliminate spurious periodic interaction in the direction normal to the surfaces[31].

AIMD simulations. In this study, the AIMD simulations are performed within the framework of DFT with the Generalized Gradient Approximation (GGA) using the Perdew-Burke-Ernzerhof (PBE)[47] functional and Grimme D3 correction[48] that is implemented in the CP2K/Quickstep code[49]. The core electrons are described by Goedecker-Teter-Hutter (GTH) pseudopotentials[50,51], and the valence electrons are described by a mixed Gaussian and Plane Waves (GPW) basis[52]. The wave functions are expanded on a Double-Zeta Valence Polarized (DZVP) basis set along with an auxiliary plane wave basis set at a cutoff energy of 400 Ry. During AIMD, the nuclei are treated within the Born-Oppenheimer approximation with a timestep of 0.5 fs for equilibrium simulation, while 1 fs for metadynamics simulations with the replacement of hydrogen by deuterium to

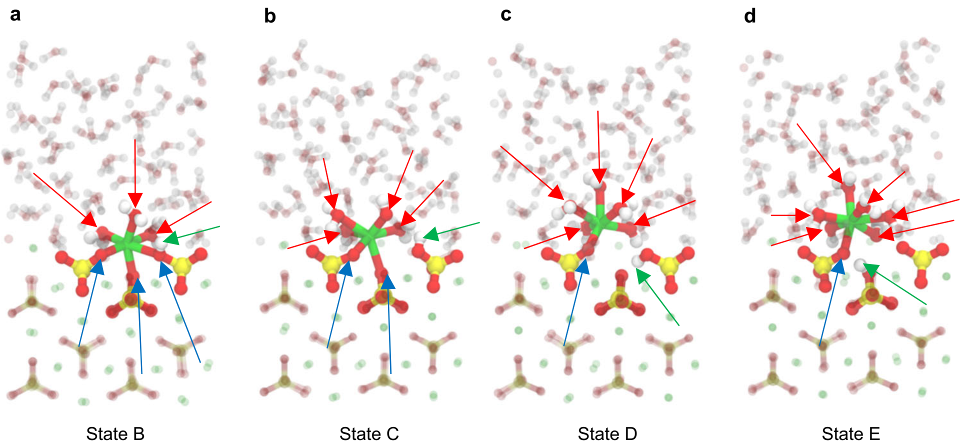

Fig. 7 AIMD simulation snapshots for Ca-olivine dissolution. **a** State B, **b** State C, **c** State D, and **d** State E from Ca-olivine dissolution. See Table 2 for the CNs of each state. The atom colors are Ca = green; Si = yellow; O = red; H = white. The surface Ca atom with bonded surface silicate ions and water molecules are drawn in solid colors while other atoms are drawn in transparent colors. The red, blue, and green arrows show the Ca-O_w, Ca-O_s, and O_s-H bonds, respectively.

accelerate the structural evolution without energy drifts[53,54]. The temperature is maintained at 300 K using a Nose-Hoover thermostat[55,56] coupled to the system with a time constant of 100 fs in the Canonical ensemble (*NVT*). All the systems are first optimized to a stable state and thermalized for at least 5 ps before the metadynamics production runs. The metadynamics for the dissolutions of Mg-olivine and Ca-olivine are run for 336 ps and 186 ps, respectively. The 336 ps and 186 ps AIMD simulations are performed using 32 nodes on cluster with 16 cores per node (totally 512 cores) for around 2 calendar months with the computation efficiency of around 10 ps per day.

Metadynamics enhanced sampling. With the well-tempered metadynamics simulations[57], I use three-dimensional collective variables (CVs) characterized by the CNs to monitor the dissolution process: (1) The CN(Mg-O_s) or CN(Ca-O_s) are the CNs of the specified Mg or Ca ion with the olivine surface silicate oxygen atoms (see Fig. 1 for the Mg-olivine case). (2) The CN(Mg-O_w) or CN(Ca-O_w) are the CNs of the specified Mg or Ca ion with oxygen atoms from water molecules. (3) The CN(O_s-H) is the coordination number of the olivine surface silicate oxygen atoms with protonation from water hydrogens. As defined in the CP2K implementation[58], the CN between X and Y atoms have the expression as follows:

$$\mathrm{CN(X\text{-}Y)} = \frac{1}{N_{\mathrm{X}}}\Sigma_{i_{\mathrm{X}}}\Sigma_{j_{\mathrm{Y}}}\frac{1-\left(\frac{r_{ij}}{R_0}\right)^{nn}}{1-\left(\frac{r_{ij}}{R_0}\right)^{nd}}, \tag{3}$$

where N_{X} is the number of atom X, r_{ij} is the distance between the *i*th X atom and the *j*th Y atom, $nn = 16$ and $nd = 32$ are parameters that control the curvature of the function, and R_0 is the reference X-Y distances that I use $R_0 = 2.8$ Å for calculating CN(Mg-O_s) and CN(Mg-O_w), $R_0 = 3.2$ Å for calculating CN(Ca-O_s) and CN(Ca-O_w), and $R_0 = 1.3$ Å for calculating CN(O_s-H). The Gaussian hills are deposited every 30 timesteps with the initial height of 2.5 kJ mol^{-1} and width of 0.2 for CN(Mg-O_s), CN(Mg-O_w), CN(Ca-O_s), and CN(Ca-O_w), and 0.067 for CN(O_s-H). The bias factors are 30 for Mg-olivine and 20 for Ca-olivine dissolution simulations. Finally, the minimum free energy paths identified from the final 3D free energy surfaces are analyzed using the MEPSAnd software package[59]. Note similar procedure has been used to study the dissolution of tricalcium silicate (the main component in ordinary Portland cement) in the context of understanding the durability and mechanical property of concrete[60].

Data availability

The input files for running AIMD metadynamics simulations using CP2K (https://www.cp2k.org/) as well as simulation outputs analyzed in this study are available at https://doi.org/10.5281/zenodo.8380287.

Received: 10 May 2023; Accepted: 28 September 2023;
Published online: 09 October 2023

References

1. Bourg, I. C., Beckingham, L. E. & DePaolo, D. J. The nanoscale basis of CO_2 trapping for geologic storage. *Environ. Sci. Technol.* **49**, 10265–10284 (2015).
2. Kelemen, P., Benson, S. M., Pilorgé, H., Psarras, P. & Wilcox, J. An overview of the status and challenges of CO_2 storage in minerals and geological formations. *Front. Climate* **1**, 9 (2019).
3. Snæbjörnsdóttir, S. Ó. et al. Carbon dioxide storage through mineral carbonation. *Nat. Rev. Earth Environ.* **1**, 90–102 (2020).
4. Raza, A., Glatz, G., Gholami, R., Mahmoud, M. & Alafnan, S. Carbon mineralization and geological storage of CO_2 in basalt: Mechanisms and technical challenges. *Earth-Sci. Rev.* **229**, 104036 (2022).
5. O'Connor, W. K., Dahlin, D. C., Rush, G., Dahlin, C. L. & Collins, W. K. Carbon dioxide sequestration by direct mineral carbonation: process mineralogy of feed and products. *Min. Metall. Explor.* **19**, 95–101 (2002).
6. Saldi, G. D., Schott, J., Pokrovsky, O. S., Gautier, Q. & Oelkers, E. H. An experimental study of magnesite precipitation rates at neutral to alkaline conditions and 100–200 C as a function of pH, aqueous solution composition and chemical affinity. *Geochim. Cosmochim. Acta* **83**, 93–109 (2012).
7. Miller, Q. R. et al. Anomalously low activation energy of nanoconfined $MgCO_3$ precipitation. *Chem. Commun.* **55**, 6835–6837 (2019).
8. Wang, F., Dreisinger, D., Jarvis, M. & Hitchins, T. Kinetics and mechanism of mineral carbonation of olivine for CO_2 sequestration. *Miner. Eng.* **131**, 185–197 (2019).
9. Miller, Q. R. et al. Emerging investigator series: Ion diffusivities in nanoconfined interfacial water films contribute to mineral carbonation thresholds. *Environ. Sci. Nano* **7**, 1068–1081 (2020).
10. Kerisit, S. N., Mergelsberg, S. T., Thompson, C. J., White, S. K. & Loring, J. S. Thin water films enable low-temperature magnesite growth under conditions relevant to geologic carbon sequestration. *Environ. Sci. Technol.* **55**, 12539–12548 (2021).
11. Calcara, M. & Caricaterra, M. CO_2 dipole moment: a simple model and its implications for CO_2-rock interactions. *Minerals* **13**, 87 (2023).
12. Regnault, O., Lagneau, V. & Schneider, H. Experimental measurement of portlandite carbonation kinetics with supercritical CO_2. *Chem. Geol.* **265**, 113–121 (2009).

13. Matter, J. M. et al. Rapid carbon mineralization for permanent disposal of anthropogenic carbon dioxide emissions. *Science* **352**, 1312–1314 (2016).
14. Snæbjörnsdóttir, S. Ó. et al. The chemistry and saturation states of subsurface fluids during the in situ mineralisation of CO_2 and H_2S at the CarbFix site in SW-Iceland. *Int. J. Greenh. Gas Control* **58**, 87–102 (2017).
15. Trias, R. et al. High reactivity of deep biota under anthropogenic CO_2 injection into basalt. *Nat. Comm.* **8**, 1063 (2017).
16. Pogge von Strandmann, P. A. et al. Rapid CO_2 mineralisation into calcite at the CarbFix storage site quantified using calcium isotopes. *Nat. Comm.* **10**, 1983 (2019).
17. McGrail, B. P., Spane, F. A., Amonette, J. E., Thompson, C. & Brown, C. F. Injection and monitoring at the Wallula basalt pilot project. *Energy Procedia* **63**, 2939–2948 (2014).
18. McGrail, B. P. et al. Field validation of supercritical CO_2 reactivity with basalts. *Environ. Sci. Technol. Lett.* **4**, 6–10 (2017).
19. McGrail, B. P. et al. Wallula basalt pilot demonstration project: Post-injection results and conclusions. *Energy Procedia* **114**, 5783–5790 (2017).
20. Aradóttir, E., Sonnenthal, E. & Jónsson, H. Development and evaluation of a thermodynamic dataset for phases of interest in CO_2 mineral sequestration in basaltic rocks. *Chem. Geol.* **304**, 26–38 (2012).
21. Aradóttir, E., Sonnenthal, E., Björnsson, G. & Jónsson, H. Multidimensional reactive transport modeling of CO_2 mineral sequestration in basalts at the Hellisheidi geothermal field. *Iceland. Int. J. Greenh. Gas Control* **9**, 24–40 (2012).
22. Alfredsson, H. A. et al. The geology and water chemistry of the Hellisheidi, SW-Iceland carbon storage site. *Int. J. Greenh. Gas Control* **12**, 399–418 (2013).
23. Jayne, R. S., Wu, H. & Pollyea, R. M. Geologic CO_2 sequestration and permeability uncertainty in a highly heterogeneous reservoir. *Int. J. Greenh. Gas Control* **83**, 128–139 (2019).
24. Wu, H., Jayne, R. S., Bodnar, R. J. & Pollyea, R. M. Simulation of CO_2 mineral trapping and permeability alteration in fractured basalt: Implications for geologic carbon sequestration in mafic reservoirs. *Int. J. Greenh. Gas Control* **109**, 103383 (2021).
25. Criscenti, L. J. & Cygan, R. T. Molecular simulations of carbon dioxide and water: cation solvation. *Environ. Sci. Technol.* **47**, 87–94 (2013).
26. Abdolhosseini Qomi, M. J. et al. Molecular-scale mechanisms of CO_2 mineralization in nanoscale interfacial water films. *Nat. Rev. Chem.* **6**, 598–613 (2022).
27. Zhang, S. & DePaolo, D. J. Rates of CO_2 mineralization in geological carbon storage. *Acc. Chem. Res.* **50**, 2075–2084 (2017).
28. Kastanidis, P. et al. Solubility of methane and carbon dioxide in the aqueous phase of the ternary (methane + carbon dioxide + water) mixture: experimental measurements and molecular dynamics simulations. *J. Chem. Eng. Data* **63**, 1027–1035 (2018).
29. Omrani, S., Ghasemi, M., Mahmoodpour, S., Shafiei, A. & Rostami, B. Insights from molecular dynamics on CO_2 diffusion coefficient in saline water over a wide range of temperatures, pressures, and salinity: CO_2 geological storage implications. *J. Mol. Liq.* **345**, 117868 (2022).
30. Casey, W. H. & Westrich, H. R. Control of dissolution rates of orthosilicate minerals by divalent metal–oxygen bonds. *Nature* **355**, 157–159 (1992).
31. Kerisit, S., Bylaska, E. J. & Felmy, A. R. Water and carbon dioxide adsorption at olivine surfaces. *Chem. Geol.* **359**, 81–89 (2013).
32. Gunnarsson, I. et al. The rapid and cost-effective capture and subsurface mineral storage of carbon and sulfur at the CarbFix2 site. *Int. J. Greenh. Gas Control* **79**, 117–126 (2018).
33. Sigfússon, B. et al. Reducing emissions of carbon dioxide and hydrogen sulphide at Hellisheidi power plant in 2014-2017 and the role of CarbFix in achieving the 2040 Iceland climate goals. *Energy Procedia* **146**, 135–145 (2018).
34. Goldberg, D. et al. Geological storage of CO_2 in sub-seafloor basalt: The CarbonSAFE pre-feasibility study offshore Washington State and British Columbia. *Energy Procedia* **146**, 158–165 (2018).
35. Sullivan, M., Rodosta, T., Mahajan, K. & Damiani, D. An overview of the Department of Energy's CarbonSAFE Initiative: Moving CCUS toward commercialization. *AlChE J* **66**, e16855 (2020).
36. Zhang, S., DePaolo, D. J., Xu, T. & Zheng, L. Mineralization of carbon dioxide sequestered in volcanogenic sandstone reservoir rocks. *Int. J. Greenh. Gas Control* **18**, 315–328 (2013).
37. Zhang, S. & Liu, H.-H. Porosity–permeability relationships in modeling salt precipitation during CO_2 sequestration: Review of conceptual models and implementation in numerical simulations. *Int. J. Greenh. Gas Control* **52**, 24–31 (2016).
38. Zhang, S., Liu, H.-H., Van Dijke, M. I., Geiger, S. & Agar, S. M. Constitutive relations for reactive transport modeling: Effects of chemical reactions on multi-phase flow properties. *Transport. Porous. Med.* **114**, 795–814 (2016).
39. Sanna, A., Uibu, M., Caramanna, G., Kuusik, R. & Maroto-Valer, M. A review of mineral carbonation technologies to sequester CO_2. *Chem. Soc. Rev.* **43**, 8049–8080 (2014).
40. Gadikota, G. Multiphase carbon mineralization for the reactive separation of CO_2 and directed synthesis of H_2. *Nat. Rev. Chem.* **4**, 78–89 (2020).
41. Rim, G. et al. CO_2 utilization in built environment via the PCO_2 swing carbonation of alkaline solid wastes with different mineralogy. *Faraday Discuss* **230**, 187–212 (2021).
42. La Plante, E. C. et al. Controls on CO_2 mineralization using natural and industrial alkaline solids under ambient conditions. *ACS Sustain. Chem. Eng.* **9**, 10727–10739 (2021).
43. Watson, G., Oliver, P. & Parker, S. Computer simulation of the structure and stability of forsterite surfaces. *Phys. Chem. Miner.* **25**, 70–78 (1997).
44. De Leeuw, N., Parker, S., Catlow, C. & Price, G. Modelling the effect of water on the surface structure and stability of forsterite. *Phys. Chem. Miner.* **27**, 332–341 (2000).
45. Prigiobbe, V., Suarez Negreira, A. & Wilcox, J. Interaction between olivine and water based on density functional theory calculations. *J. Phys. Chem. C* **117**, 21203–21216 (2013).
46. Demouchy, S. Defects in olivine. *Eur. J. Miner.* **33**, 249–282 (2021).
47. Perdew, J. P., Burke, K. & Ernzerhof, M. Generalized gradient approximation made simple. *Phys. Rev. Lett.* **77**, 3865 (1996).
48. Grimme, S., Antony, J., Ehrlich, S. & Krieg, H. A consistent and accurate ab initio parametrization of density functional dispersion correction (DFT-D) for the 94 elements H-Pu. *J. Chem. Phys.* **132**, 154104 (2010).
49. VandeVondele, J. et al. Quickstep: fast and accurate density functional calculations using a mixed Gaussian and plane waves approach. *Comput. Phys. Commun.* **167**, 103–128 (2005).
50. Goedecker, S., Teter, M. & Hutter, J. Separable dual-space Gaussian pseudopotentials. *Phys. Rev. B* **54**, 1703 (1996).
51. Hartwigsen, C., Gœdecker, S. & Hutter, J. Relativistic separable dual-space Gaussian pseudopotentials from H to Rn. *Phys. Rev. B* **58**, 3641 (1998).
52. VandeVondele, J. & Hutter, J. Gaussian basis sets for accurate calculations on molecular systems in gas and condensed phases. *J. Chem. Phys.* **127**, 114105 (2007).
53. Leung, K. & Rempe, S. B. Ab initio rigid water: Effect on water structure, ion hydration, and thermodynamics. *Phys. Chem. Chem. Phys.* **8**, 2153–2162 (2006).
54. Claverie, J., Bernard, F., Cordeiro, J. M. M. & Kamali-Bernard, S. Ab initio molecular dynamics description of proton transfer at water-tricalcium silicate interface. *Cem. Concr. Res.* **136**, 106162 (2020).
55. Martyna, G. J., Klein, M. L. & Tuckerman, M. Nosé–Hoover chains: The canonical ensemble via continuous dynamics. *J. Chem. Phys.* **97**, 2635–2643 (1992).
56. Nosé, S. A molecular dynamics method for simulations in the canonical ensemble. *Mol. Phys.* **52**, 255–268 (1984).
57. Bonomi, M. & Parrinello, M. Enhanced sampling in the well-tempered ensemble. *Phys. Rev. Lett.* **104**, 190601 (2010).
58. Kühne, T. D. et al. CP2K: An electronic structure and molecular dynamics software package-Quickstep: Efficient and accurate electronic structure calculations. *J. Chem. Phys.* **152**, 194103 (2020).
59. Marcos-Alcalde, I., López-Viñas, E. & Gómez-Puertas, P. MEPSAnd: Minimum energy path surface analysis over n-dimensional surfaces. *Bioinformatics* **36**, 956–958 (2020).
60. Li, Y., Pan, H., Liu, Q., Ming, X. & Li, Z. Ab initio mechanism revealing for tricalcium silicate dissolution. *Nat. Comm.* **13**, 1253 (2022).

Acknowledgements

I thank Dr. Byoungseon Jeon from Aramco Research Center – Boston, Strategic Modeling Team, for high performance computing (HPC) support.

Author contributions

H.C. performed the research and wrote the paper.

Competing interests

The author declares no competing interests.

Additional information

Supplementary information The online version contains supplementary material available at https://doi.org/10.1038/s43247-023-01028-5.

Correspondence and requests for materials should be addressed to Hsieh Chen.

Peer review information *Communications Earth & Environment* thanks Massimo Calcara and the other, anonymous, reviewer(s) for their contribution to the peer review of this work. Primary Handling Editors: Sadia Ilyas and Joe Aslin. A peer review file is available.

Reprints and permission information is available at http://www.nature.com/reprints

Publisher's note Springer Nature remains neutral with regard to jurisdictional claims in published maps and institutional affiliations.

Open Access This article is licensed under a Creative Commons Attribution 4.0 International License, which permits use, sharing, adaptation, distribution and reproduction in any medium or format, as long as you give appropriate credit to the original author(s) and the source, provide a link to the Creative Commons licence, and indicate if changes were made. The images or other third party material in this article are included in the article's Creative Commons licence, unless indicated otherwise in a credit line to the material. If material is not included in the article's Creative Commons licence and your intended use is not permitted by statutory regulation or exceeds the permitted use, you will need to obtain permission directly from the copyright holder. To view a copy of this licence, visit http://creativecommons.org/licenses/by/4.0/.

© The Author(s) 2023